Nanoindentation of ion-irradiated reactor pressure vessel steels – model-based interpretation and comparison with neutron irradiation

Röder, F.; Heintze, C.; Pecko, S.; Akhmadaliev, S.; Bergner, F.; Ulbricht, A.; Altstadt, E.;

Originally published:

January 2018

Philosophical Magazine 98(2018)11, 911-933

DOI: https://doi.org/10.1080/14786435.2018.1425007

Nanoindentation of ion-irradiated reactor pressure vessel steels – model-based interpretation and comparison with neutron irradiation

F. Röder[a], C. Heintze[a], S. Pecko[b], S. Akhmadaliev[c], F. Bergner[a], A. Ulbricht[a], and E. Altstadt[a]

a) *Helmholtz-Zentrum Dresden-Rossendorf, Institut für Ressourcenökologie, Bautzner Landstr. 400, D-01328 Dresden, Germany*

b) *Institute of Nuclear and Physical Engineering, Slovak University of Technology, Ilkovičova 3, 81219 Bratislava, Slovakia*

c) *Helmholtz-Zentrum Dresden-Rossendorf, Institut für Ionenstrahlphysik und Materialforschung, Bautzner Landstr. 400, D-01328 Dresden, Germany*

Corresponding author e-mail: F.Bergner@hzdr.de

Nanoindentation of ion-irradiated reactor pressure vessel steels – model-based interpretation and comparison with neutron irradiation

Ion-irradiation-induced hardening is investigated on six selected reactor pressure vessel (RPV) steels. The steels were irradiated with 5 MeV Fe^{2+} ions at fluences ranging from 0.01 to 1.0 displacements per atom (dpa) and the induced hardening of the surface layer was probed with nanoindentation. To separate the indentation size effect and the substrate effect from the irradiation-induced hardness profile, we developed an analytic model with the plastic zone of the indentation approximated as a half sphere. This model allows the actual hardness profile to be retrieved and the measured hardness increase to be assigned to the respective fluence. The obtained values of hardness increase versus fluence are compared for selected pairs of samples in order to extract effects of the RPV steel composition. We identify hardening effects due to increased levels of copper, manganese-nickel and phosphorous. Further comparison with available neutron-irradiated conditions of the same heats of RPV steels indicates pronounced differences of the considered effects of composition for irradiation with neutrons versus ions.

Keywords: nanoindentation; plastic zone; ion irradiation; neutron irradiation; reactor pressure vessel steel; irradiation hardening

1. Introduction

Reactor pressure vessel (RPV) steels degrade due to the exposure to fission neutrons [1-3]. This paper deals with RPV steels exposed to self-ion irradiation, which is expected to provide further insight into basic details of irradiation damage [4-7]. While the assignment of a neutron exposure, e.g. in units of displacements per atom (dpa), to a measured mechanical property, e.g. Vickers hardness, is straightforward for neutron-irradiated samples, the same type of assignment is far from trivial for ion-irradiated samples. In contrast to neutron irradiation, the ion exposure is heavily graded and confined to a layer of a thickness of the order of 1 μm. This requires nanoindentation be performed [8-10], which in turn integrates over a plastically deformed volume of graded

exposure.

Results of studies on ion-irradiated RPV steels and related model alloys were reported in [11-20]. Proton irradiation was addressed in [21]. These studies are focused on the nature and behavior of ion-irradiation-induced (below in short: ion-induced) defect and solute atom clusters and provide microstructural evidence, mainly by means of TEM. Nanoindentation was used to estimate the ion-induced hardening [11,13-17]. The comparison of hardening of RPV steels caused by irradiations with ions and neutrons was not explicitly addressed until recently [17].

Different approaches were applied to assign measured hardness values to dpa levels. Fujii et al. [13] plotted the indentation hardness obtained for an indentation depth of 150 nm as function of the dose calculated for a depth of 300 nm. Watanabe et al. [14,17] applied an approach to hardness that ignores the graded nature of damage. Yabuuchi et al. [15] considered the nominal dpa level at a depth of 600 nm (for peak damage that occurred at a depth of 1.5 μm), whereas the indentation depth was not specified. Jin et al. [16] reported the peak dpa level at 1.8 μm. The indentation hardness as function of indentation depth did not show a clear trend for the depth range from 0.2 to 1.4 μm. None of these studies considered the separation of the ion-irradiation effect on hardness and the indentation size effect (ISE) in detail. More advanced strategies for the evaluation of nanoindentation results on ion-irradiated metals are based on segmental fits of the Nix-Gao relation [22], which inherently assumes step-like hardness profiles [23-25].

The first objective of the present paper is to outline an approach aimed to separate the ion-irradiation effect from the indentation size effect and to properly assign hardness values to dpa levels. Especially single-step irradiations result in inhomogeneous damage profiles leading to a so-called "damage grade effect" [26],

which was addressed in recent work [27,28]. The approach suggested in [28] represents the plastic zone size as a function of the local yield stress, which in turn is a function of the dpa profile. The indentation size effect was not considered. Xiao et al. [27] take into account both the indentation size effect and the variation of the dislocation density within the plastic zone. Neither of these approaches in the present form does provide the depth profile of the actual hardness, which is, however, necessary for our purposes.

The separation of the ion-irradiation effect and the assignment of hardness values to dpa levels are relevant for different materials including RPV steels and ferritic/martensitic steels. Here, we provide experimental results for a number of RPV steels self-ion-irradiated in the range from 0.01 to 1 dpa. The set of RPV steels was selected on the basis of two criteria, namely (1) the availability of pairs of steels exhibiting interesting differences of the steel composition and (2) the availability of well characterized neutron-irradiated counterparts of the same heats of steels [29-33]. In order to specify the meaning of "interesting differences of composition", we refer to the case of neutron irradiation. It is state of the art in this context that the impurity elements Cu and P as well as the alloying elements Mn and Ni are crucial for the evolution of the microstructure and mechanical properties of RPV steels under neutron irradiation [2,34].

The second objective of the present paper is to identify effects of composition, in particular Cu, P and Mn-Ni, of selected RPV steels exposed to ion irradiation. These effects have been addressed in the literature only in few cases [13,15,17].

The structure of this paper is as follows: In the experimental section, we introduce the steels of concern and describe the irradiation and nanoindentation experiments in detail. In the subsequent section, we develop an analytic model for the indentation hardness as a function of depth based on the damage profile, which permits

to disentangle the actual hardness from the indentation size and softer substrate effect. In the results section, we consider the model-based hardness retrieval at the example of a selected steel and present the ion-induced hardness increase as a function of the fluence for all introduced RPV steels. In the discussions section, we compare in detail the ion-irradiation results with respect to Cu, P and Mn-Ni effects. We further compare the effects of the mentioned impurity and alloying elements on the ion-induced hardening with the effects of the same chemical elements on the neutron-induced Vickers hardness increase measured for the same materials.

2. Experiment

2.1 Selected materials and sample preparation

The investigated RPV steels are detailed with respect to manufacturing and composition in Tables 1 and 2, respectively. The data were taken from [29,33,35,36]. All materials of this study are base metals. JFL and JRQ are Japanese commercial-grade RPV steels originating from IAEA coordinated research programs [35]. These steels contain similar amounts of Mn and Ni, but differ with respect to the product form, Cu content and P content. JPB and JPC are Japanese A533B-cl.1 type model steels also provided for IAEA coordinated research programs. Both are of low Cu content and differ only with respect to the P content. ANP-4 is a 22NiMoCr3-7 type RPV steel provided by AREVA GmbH, Erlangen (Germany). Its Mn content is lower than for JFL and JRQ, whereas the Cu content is in between. GW8 is a Russian type 15Kh2MFAA RPV steel manufactured by Skoda Works (Czech Republic). Relatively high Cr and V as well as low Mn and Ni concentrations characterize this type of steel. It was taken from the virgin RPV of unit 8 of the decommissioned NPP Greifswald (Germany). For each material, we prepared samples of 10mm x 10mm x 1mm size with mechanically

polished surfaces (1 μm diamond suspension).

Table 1. Details on the RPV steels investigated in this study. The abbreviations w.c., a.c., c.f., and o.q. denote water cooled, air cooled, cooled in furnace, and oil quenched, respectively.

Material	Code	Product	Final heat treatment	Manufacturer
A508 cl. 3	JFL	forging	880°C/9h, w.c., 640°C/9h, a.c.	Kawasaki Steel Corp., Japan
A533B cl. 1 model steels	JPB JPC	plate	880°C/1h, a.c., 670°C/80min, a.c.	Nippon Steel Corp., Japan
A533B cl. 1	JRQ	plate	880°C, w.c., 665°C/12h, 620°C/40h	Kawasaki Steel Corp., Japan
22NiMoCr3-7	ANP-4	forging	890°C/4h, w.c., 650°C/7h, a.c.	Japan Steel Works, Japan
15Kh2MFAA	GW8	forging	1000°C, o.q., 680°C-720°C, a.c., 665°C/31-90h, c.f.	Škoda, Czech Republic

Table 2. Composition of the considered RPV steels in wt % (balance Fe).

Code	C	Mn	Si	Cr	Ni	Mo	V	P	Cu
JFL	0.17	1.44	0.25	0.20	0.75	0.51	0.004	0.004	0.01
JRQ	0.18	1.42	0.24	0.12	0.84	0.51	0.002	0.017	0.14
JPB	0.20	1.42	0.26	0.15	0.83	0.54	0.01	0.017	0.01
JPC	0.18	1.45	0.27	0.15	0.81	0.54	0.01	0.007	0.01
ANP-4	0.21	0.85	0.22	0.39	0.84	0.55	-	0.006	0.05
GW8	0.15	0.45	0.30	2.86	0.1	0.79	0.30	0.008	0.048

2.2 Ion-irradiation experiment

The ion irradiation was performed at the Ion Beam Center (IBC) of Helmholtz-Zentrum Dresden-Rossendorf (HDZR), Dresden (Germany). For each of the selected materials, five samples have been irradiated with Fe^{2+} ions at 5 MeV at 300°C at different fluences yielding a number of different exposures at a depth of 500 nm of 0.01, 0.03, 0.1, 0.3, and 1.0 dpa, where the amount of implanted self-ions is less than 10^{-5} ions per atom at 1 dpa. The corresponding fluences have been determined by SRIM calculations [37] following the procedure given in [38] with a displacement energy of 40 eV for a pure Fe

target according to the ASTM standard E521. The resulting dpa and implantation profiles are presented in Figure 1. The irradiations have been performed at nearly the same flux (10^{11} $cm^{-2}s^{-1}$) in single step mode with scanning the focussed beam in normal incidence to the polished sample surface. The irradiation times and measured currents are compiled in Table 3.

Table 3. Irradiation parameters.

Exposure (dpa)	Exposure (10^{14} cm^{-2})	Beam current (nA)	Irradiation time
0.01	0.27	70	8 min
0.03	0.80	130	13 min
0.1	2.66	100-120	1 h
0.3	7.98	130-140	2 h 20 min
1	26.6	120-160	8 h 30 min

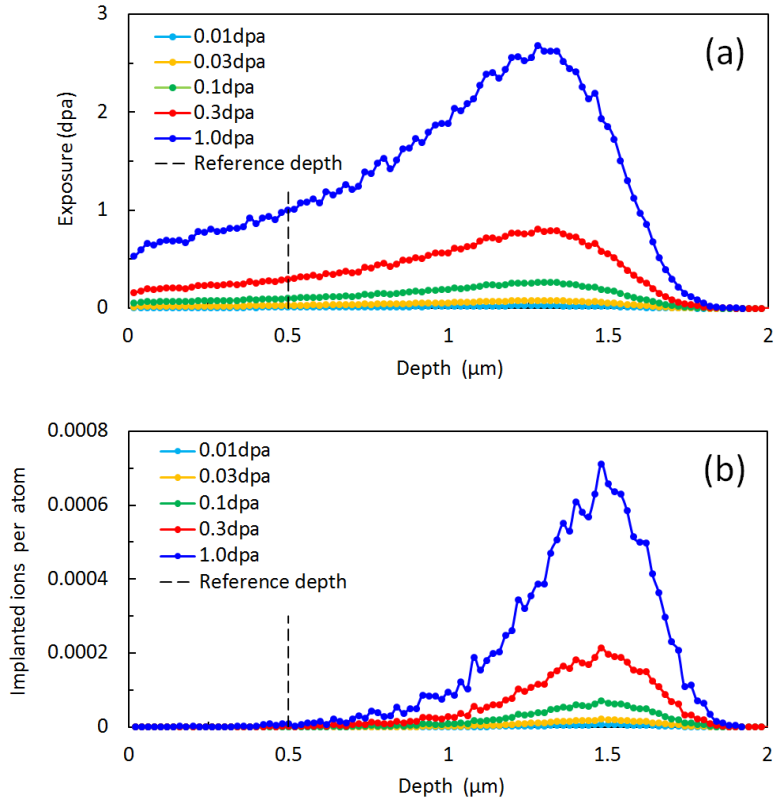

Figure 1. Exposure (a) and number of implanted ions per lattice atom (b) as functions of the depth for different ion beam fluences determined using SRIM calculations. The nominal dpa values 0.01, 0.03, 0.1, 0.3, and 1.0 were taken at a depth of 500 nm (see Table 3).

2.3 Nanoindentation

The nanoindentation testing was conducted by means of the Universal Nanomechanical Tester (UNAT, ASMEC GmbH) equipped with a Berkovich indenter. The area function of the indenter has been calibrated by means of fused silica and sapphire with known bulk moduli. We employed a load cycle as plotted in Figure 2. A maximum load of F_{max}=50 mN yields a contact depth of approximately 1 µm. For each sample, we chose an indentation pattern of 6x6 individual indents separated by a spacing of 50 µm. The Quasi Continuous Stiffness Measurement (QCSM) module of ASMEC was applied to enable the measurement of the indentation hardness as a function of ontact depth. At each load point, the load increase was paused for 3 s while overlaid by a sinusoidal oscillation. This permits a precise determination of the contact stiffness for each load point, which is necessary for eliminating the contribution of the elastic deformation of the surface and for determining the contact depth. Thermal drift was estimated by fitting the slope of the displacement signal as a function of time during holding at 5 mN, and corrected subsequently. The zero point of the load-displacement curve was extrapolated by fitting the model of a Hertzian contact to the measured load-displacement curve for a depth range of a few 10 nm. Hardness and indentation moduli were calculated from the mean load displacement curves, which were computed by averaging individual load displacement curves after removal of outliers. The error bars are standard deviations of the mean values and were determined by error propagation.

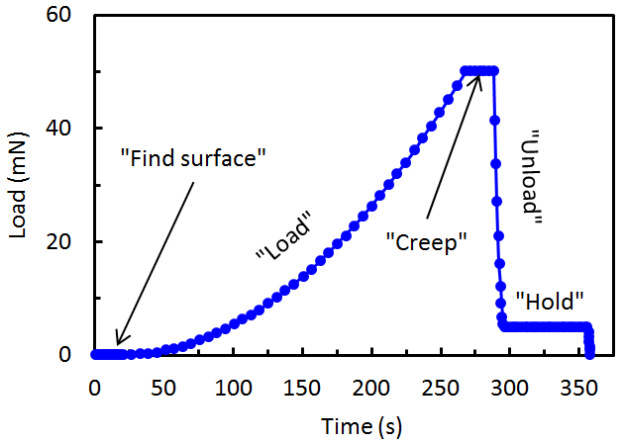

Figure 2. Load cycle for the QCS measurements. The "Find surface" segment was used for zero-point correction and "Hold" for thermal drift correction. Each point in the "Load" segment was overlaid by a sinusoidal oscillation.

3. Modelling

The plastic indentation of the indenter tip into the surface forces geometrically necessary dislocations, which strongly influence the hardness measurement, especially at small contact depth. In the frame of strain gradient plasticity [24], the indentation hardness H_{IT} probed by a conical indenter grows with decreasing contact depth h_{c} as

$$H_{\mathrm{IT}}(h_c) = H_0\sqrt{1+\frac{h^*}{h_{\mathrm{c}}}} \qquad (1)$$

We distinguish between the actual hardness H_0 as a pure material property and the indentation hardness $H_{\mathrm{IT}}(h_{\mathrm{c}})$, which depends on the measurement set-up. In the frame of the Taylor dislocation model, the hardness H_0 is related to the density of the statistically stored dislocations. The characteristic length h^* depends on the ratio of elastic modulus and hardness H_0 [39] but also on the cone angle of the indenter [22]. This model describes the indentation hardness profile for homogeneous bulk materials.

To consider an inhomogeneous hardness distribution, we develop the following analytic half-sphere model: Similar to the considerations in [28], we describe the profile

of the actual (local) hardness $H_0(z)$ as a function of the inhomogeneous dpa-profile $\Phi(z)$:

$$H_0(z) = H_S + \alpha[\Phi(z)]^n \quad (2)$$

Here, we assume a linear superposition of the hardness of the unirradiated substrate H_S with the irradiation-induced hardness increase. The latter is described by a power-law function of the dpa-profile $\Phi(z)$ as suggested by Byun and Farrell [40]. For the low fluence regime, $n = 0.5$ was found corresponding to the dispersed-barrier hardening model. At larger fluences, n decreases down to 0.1, which is attributed to the saturation of the defect cluster densities. An exponent close to zero reflects the assumption of a step-like hardness profile with α as the value for the total hardness increase.

To derive a relation between the depth-dependent actual hardness and the measured hardness for a given contact depth, we first have to average the actual hardness over the plastic zone. This kind of averaging is based on the volume law of mixture proposed by [41]. We consider the actual hardness profile $H_0(z)$ of Equation (2) averaged over a hemispherical plastic zone with radius R (Equation (3)) [22,42]. We assume this radius to be proportional to the contact depth $R(h_c) = s \cdot h_c$, with s as scale factor to be fitted to the experimental data. This factor determines the growth rate of the plastic zone during the indentation experiment. We denote the mean hardness, i.e. the hardness averaged over the plastic zone for a certain contact depth h_c, as $\langle H_0 \rangle$:

$$\langle H_0 \rangle(h_c) = \frac{3}{2R(h_c)} \int_0^{R(h_c)} \left\{1 - \frac{z^2}{[R(h_c)]^2}\right\} H_0(z) \mathrm{d}z \quad (3)$$

To further consider the indentation size effect, we modify the Nix-Gao relation by replacing the constant hardness, H_0, by the mean hardness profile $\langle H_0 \rangle(h_c)$ as

determined by Equation (3). A constant characteristic length h^* is assumed, i.e. the dependence of h^* on the mean hardness is neglected, which is reasonable for small hardness changes. Finally, the indentation hardness yields:

$$H_{\mathrm{IT}}(h_{\mathrm{c}}) = \langle H_0 \rangle (h_{\mathrm{c}}) \sqrt{1 + \frac{h^*}{h_{\mathrm{c}}}} \tag{4}$$

The analytic half-sphere model defined by Equations (2) to (4) is then fitted to the experimental data by way of variation of the parameters h^*, s, H_{S}, α, and n using a non-linear least-squares fitting routine implemented in Octave. To exclude tip-rounding artefacts [43], values below 120 nm were excluded from the fit.

4. Results

4.1 Hardness versus depth for ANP-4

The indentation hardness as a function of contact depth was measured for each of the materials and irradiation conditions as introduced in section 2 including the unirradiated references. In Figure 3, the indentation hardness profiles are plotted for ANP-4 by way of example. The experimental results shown for 0.1 to 1.0 dpa and the unirradiated case are representative for the whole set of measurements. According to the indentation size effect of a pyramidal indenter, the hardness decreases with increasing depth. Furthermore, with increasing irradiation dose, the profiles are shifted to higher hardness and exhibit a plateau with growing significance around a contact depth of 200 nm. By means of our half-sphere model, we show in the following that these plateaus are consequences of the damage profiles caused by ion irradiation.

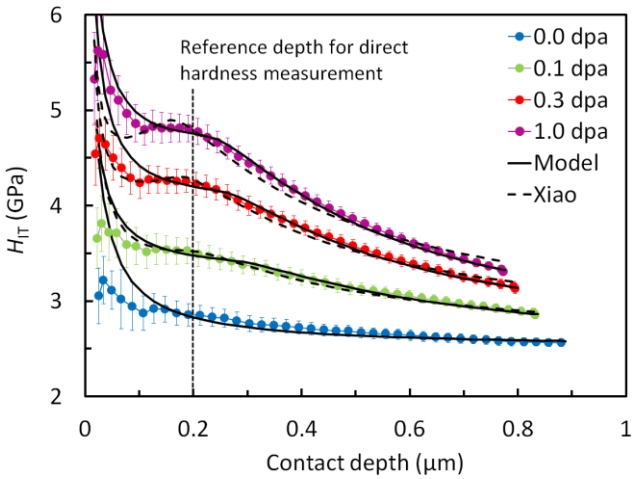

Figure 3. Indentation hardness for ANP-4 as function of the contact depth for different nominal displacement damages. The fitted curves plotted in solid black are based on the half-sphere model according to Equation (4). For comparison, the dashed curves correspond to the analytic model of Xiao *et al.* [27].

The results of the fitting procedure described above are plotted in Figure 3 as black solid lines. The fitted curves correctly describe the asymptotic behavior as well as the aforementioned plateaus within the errors of the measurements. We summarize the numerical values for the fits on the measurements of ANP-4 in Table 4 and discuss them in more detail in section 4.1.

Table 4. Fit results for ANP-4 leading to the solid curves in Figures 3 and 4. The parameters allow the investigation of both the substrate-only effect (Equation (3)) and the actual hardness profile (Equation (2)) unaffected by the indentation size and substrate effect.

Exposure (dpa)	h^* (nm)	s	H_S (GPa)	α (GPa)	n
0	55	-	2.50	-	-
0.01	58	5.8	2.32	0.57	0.001
0.03	48	5.2	2.22	0.66	0.001
0.1	29	6.9	2.40	0.93	0.04
0.3	32	7.5	2.38	1.66	0.07
1	29	8.1	2.35	2.08	0.09

Inserting the fit results of Table 4 into Equation (2) reveals the actual hardness profiles as plotted in Figure 4. These profiles are functions of the depth with respect to the real location in the material (not the contact depth) and reflect the inhomogeneous hardness because of the shape of the dpa-profiles. Compared to the dpa-profiles (Figure 1 (a)), the actual hardness appears more balanced, which might be an indication for saturation effects and/or defect diffusion. By means of the actual hardness profiles, we directly identify the hardness increase at the nominal fluence, which has been realized at 500 nm depth during the irradiation experiment (dashed vertical line in Figure 4).

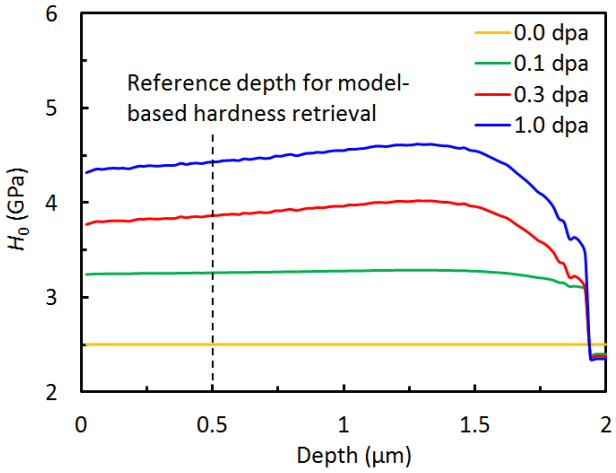

Figure 4. Actual hardness profiles for material ANP-4 (Equation 2) as functions of the depth reconstructed from the parameters determined for the fit curves in Figure 3. The hardness increase is retrieved at 500 nm (dashed line), which is the depth for the nominal displacement damage as indicated in Figure 1 (a).

Figure 5 convincingly shows a clear correlation between a direct measurement of the hardness increase at 200 nm contact depths (dashed vertical line in Figure 3) and the actual hardness value as present at 500 nm depth (Figure 4) - the reference depth for the nominal dpa values. This confirms that a direct measurement of the indentation hardness increase at 200 nm contact depth is equal to the actual hardness at the real

depth of 500 nm. There are, however, larger errors of the fit results at low dpa due to larger errors for the α parameter (Table 4). This is a matter of detectability of weak features in the indentation hardness profiles at low-dpa conditions. At larger dpa, the agreement is robust.

Additionally, we fit the recently published analytic model of Xiao et al. [27] to our measurements and plot the results as dashed curves in Figure 3. Within the error of measurement, this model also agrees well, although the features near the plateau regions appear to be slightly overswinging.

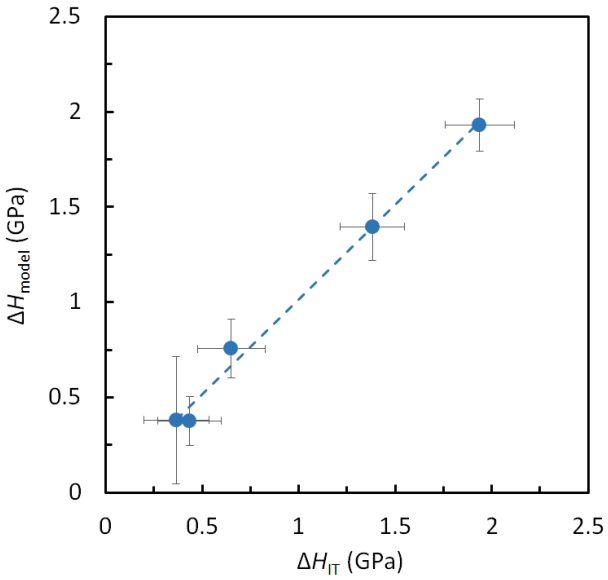

Figure 5. Correlation for ANP-4 between the directly measured indentation hardness increase ΔH_{IT} at 200 nm contact depth with the model-based hardness ΔH_{model} determined at 500 nm.

4.2 Hardness versus fluence

From the results of section 4.1, we conclude that the actual (local) hardness at a depth of 500 nm is equal to the indentation hardness measured at a contact depth of 200 nm. Simultaneously, the depth of 500 nm is the reference depth to which the ion fluences in

units of dpa (i.e. 0.01, 0.03, 0.1, 0.3, and 1) were assigned according to Figure 1 (a). Therefore, the indentation hardness measured at a contact depth of 200 nm is associated with the dpa values provided in Table 3. This equivalence is schematically presented in Figure 6.

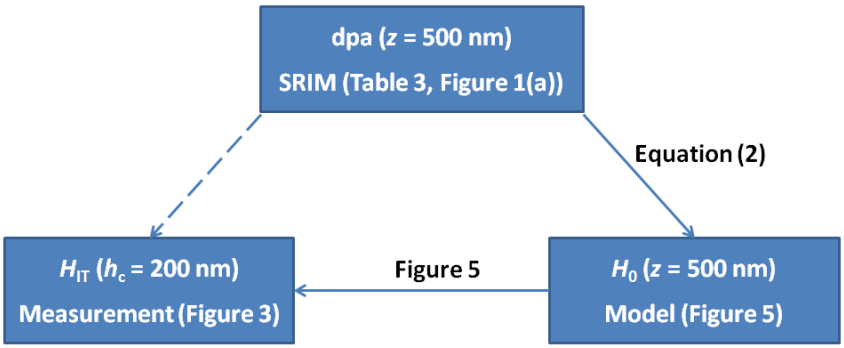

Figure 6. Scheme for the model-based assignment of the dpa values and the actual hardness at 500 nm depth with the indentation hardness measured at 200 nm.

In the following, we employ the contact depth of 200 nm as a reference depth for the evaluation of the entire experimental dataset. Figure 7 summarizes the main result of the present study in terms of indentation-hardness increase versus ion fluence in units of dpa (displacement damage). It forms a basis for the comparison of ion-induced hardening for pairs of materials with well-defined differences of the bulk composition.

Generally, increasing dpa gives rise to a growing hardness increase. The RPV steels of high Mn and Ni concentrations exhibit a stronger hardness increase of about 2 GPa at 1 dpa compared to the CrMoV steel (GW8) showing a moderate increase of about 0.8 GPa at the same fluence. In all cases, the irradiation-induced hardness increase as function of exposure can be reasonably well fitted by a power law. The power-law exponents are in the range from 0.38 to 0.52 with the exception of GW8, which exhibits a significantly smaller exponent of 0.25.

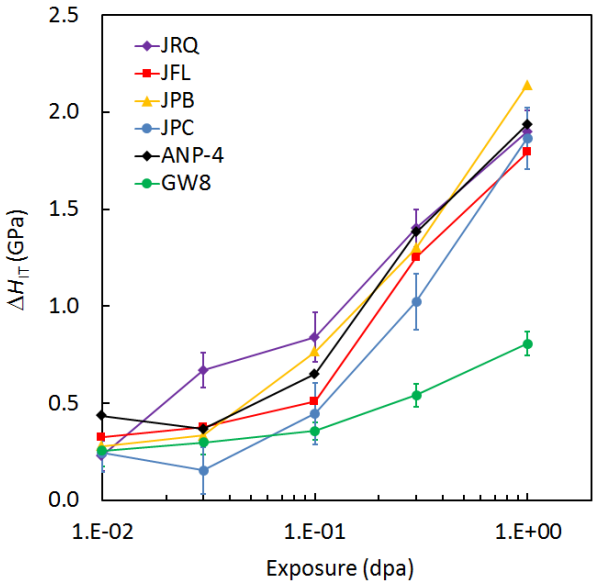

Figure 7. Actual hardness increase measured at a contact depth of 200 nm as a function of exposure (displacement damage).

5. Discussion

5.1 Model-based hardness retrieval

We discuss the fit results listed in Table 4 for the evaluation of ANP-4. For the unirradiated state, only the characteristic length h^* and the substrate hardness H_S are meaningful. The fit values obtained for h^* are of the correct order of magnitude, e.g. [10]. With increasing dpa the h^* reduces, which is anticipated because of an increasing formation of irradiation-induced defects. Following the argumentation of Hou and Jennett [44], this corresponds to a suppression of the indentation size effect by a growing structure size effect. The influence of the structure size effect becomes stronger because of a decreasing mean free path between the induced defects.

Furthermore, the scaling parameter s (i.e. the factor of proportionality between contact depth and radius of the plastic zone) is in the correct order of magnitude, but slightly decreases with decreasing dpa. This behavior seems to conflict with the fact that

harder materials tend to form smaller plastic zones [45,46] and is related to the different extensions of the plateau regions found in Figure 3. The curves suggest that lower fluences cause wider plateaus, which in turn forces the algorithm to artificially reduce the value of s.

The coefficient α describes the strength of hardness increase and grows – as expected – with increasing dpa indicating the irradiation hardening effect of interest.

The fit values of the exponent n defined according to Equation (2) are generally smaller than the value expected for real hardening-fluence dependences [40]. This may be due to saturation effects near the depth region of the damage peak, i.e. beyond the reference depth for dpa calculation. The physical significance of n must not be overstressed in the framework of a multi-parameter model.

The applied half-sphere model based on Equations (2) to (4) does add a substantial value to the interpretation of the results of the hardness measurements. Indeed, the following pieces of insight have been gained or can be gained on the basis of the model:

- The application of the half-sphere model allows the indentation size effect, the irradiation effect and the substrate effect to be separated. Here we are interested in the sole irradiation effect.
- The model provides an explanation for the observed plateau regions in the plots of indentation hardness vs. contact depth (see Figure 3). Experimental or preparation artefacts can be largely excluded as a source of the plateau.
- For the present case, the half-sphere model substantiates a link between the average hardness measured for a contact depth of 200 nm and the actual local hardness deduced for a distance of 500 nm from the sample surface.

- The model allows the hardness measured for a contact depth of 200 nm to be assigned to the dpa value calculated for a distance of 500 nm from the sample surface. It is this kind of assignment that justifies a comparison of hardness versus fluence data with reported data, e.g. for neutron-irradiated materials (see section 5.3).
- In principle, the depth-dependent actual hardness of the irradiated layer (see Figure 4) and the dpa dependence of the actual hardness can be deduced. This is not accomplished on the basis of the dislocation model of nanoindentation proposed in [27].

However, the accuracy of the model-based dpa dependence of the actual hardness is still limited as can be concluded from Figure 8. The symbols in Figure 8 were calculated by linking the model-based hardness profiles via depth z to the dpa profiles for the 0.1-, 0.3-, and 1.0-dpa irradiations. The line curve corresponds to a power law fitted to the measured hardness at a contact depth of 200 nm versus the dpa-value at 500 nm distance from the surface. Ideally, the power-law curve and the symbols should form a narrow band. On the one hand, they do not because of limitations of the model. For example, neither a purely linear superposition law nor a power-law dependence of hardness on fluence, both presumed in Equation (2), is strictly valid. Application of the model to the recovery of the fluence-dependence of hardening from indentations in only one ion-irradiated sample is, however, not within the scope of the present study. On the other hand, the intersection points of the power-law curve with the data bands formed by the symbols in Figure 8 give a consistent picture. These intersection points approximately correspond to the model-based hardening deduced for a distance of 500 nm from the surface as already indicated in Figure 5.

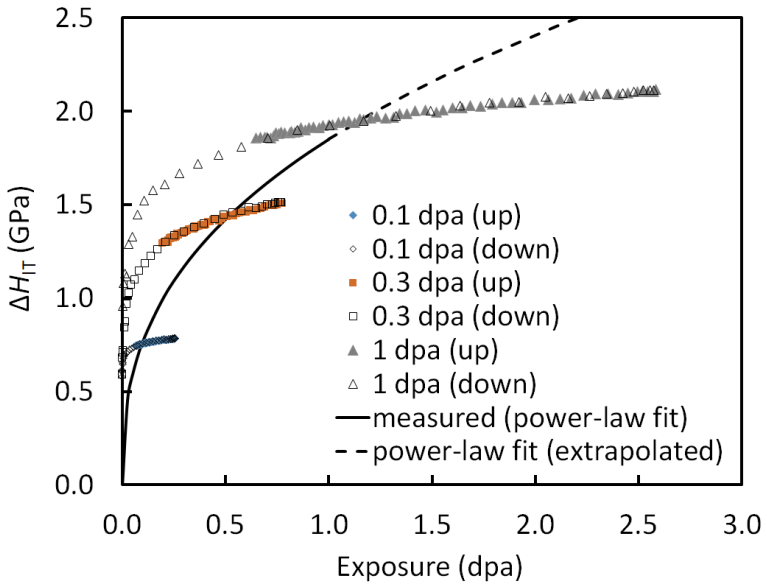

Figure 8. Model-based hardening calculated by combining Figures 1 (a) and 4 (symbols) and power-law fit of the measured hardening for ANP-4. Full and open symbols correspond to the branch of increasing and decreasing displacement damage, respectively (compare Figure 1 (a)).

5.2 Ion-irradiation-induced hardening

Since all RPV steels of this study were ion-irradiated within the same ion-irradiation run and the same procedures were applied to perform and analyze all nanoindentation experiments, the differences in the nanoindentation response presented in Figure 7 must be due to differences in the microstructure and composition of the RPV steels. Compared to major variations of the composition according to Table 2, the microstructures are considered to be sufficiently similar to exclude strong effects on the ion-irradiation response. Indeed, steel JRQ and another lot of 15Kh2MFA, for example, were reported to exhibit “only” minor morphological differences” of the microstructure, both classified as granular and lath bainite with small amounts of ferrite [47]. Dislocation densities were also reported to be similar (2.3×10^{14} m^{-2} versus 1.7×10^{14} m^{-2}) [47]. Reported differences of the carbide types can be assumed to be of

minor importance for the ion-irradiation response. It is, therefore, reasonable to consider the composition as dominant variable. Among the whole set of materials investigated, we have selected three pairs to be addressed in the discussion:

- JRQ and JPB with closest agreement of composition except for Cu (0.14 versus 0.01 wt%), but including P (0.017 wt% both),
- JPB and JPC, which are identical except for the higher P content of JPB (0.017 versus 0.007 wt%),
- ANP-4 and GW8, which are different with respect to Mn, Ni and Cr (the Cr difference being of minor importance [15]), but compare well with respect to Cu and P.

The irradiation-induced hardness increase as function of ion exposure is plotted in Figure 9 (a) to (c) for these pairs of steels. The results are discussed pair by pair below.

The hardness increase obtained for JRQ and JPB agrees for most of the fluences within experimental uncertainty noting that the standard deviation was estimated from approximately 30 repeated measurements. The overall trend in Figure 9 (a) indicates equal or insignificantly differing hardness increases in the fluence range from 0.01 to 1 dpa in spite of the strongly different Cu contents. We conclude indirectly that Cu-rich clusters cannot pose the dominant contribution to hardening. This observation confirms former results [13,17] for similar ion-irradiated steels with varied Cu content (0 – 0.2 wt%). Watanabe et al. [17] found no trend with increasing Cu below 0.05 dpa, but a weak Cu trend at exposures beyond 0.1 dpa. Our observation confirms the no-Cu-trend case even up to 1 dpa. This minor difference with [17] may be due to undocumented details in the ion irradiations. Watanabe et al. did not even observe dislocation loops

below 0.05 dpa and concluded cascade remnants to be mainly responsible for the observed hardening in this range. This conclusion and the underlying explanation may be tentatively transferred to the present situation. However, Mn and Ni might also play a role (see below). At fluences higher than 0.05 dpa loops were detected but reported to be independent of the Cu content [17]. It is necessary to note that the only statistically significant difference between JRQ and JPB in the present study was observed at 0.03 dpa. This singular observation may be due to an outlier, which requires additional verification.

In Figure 9 (b), we compare JPC and JPB, which differ exclusively with respect to the P content. The curves indicate a significant offset with more hardening found for JPB except for the lowest fluence. This offset can only be attributed to the larger P content. It appears that this kind of observation for ion-irradiated RPV steels was not reported before. If cascade remnants are assumed to be mainly responsible for hardening as suggested by Watanabe et al. [17], our finding is consistent with a stabilization of remnants by P segregation. Indeed, P has a relatively large binding energy to vacancies [48]. The agreement of the hardness increase observed for the lowest fluence then implies that there was not sufficient time for P-diffusion/segregation within the 8 min duration of the irradiation.

ANP-4 and GW8 are compared in Figure 9 (c). These RPV steels closely agree with respect to the Cu and P contents considered above, but differ significantly with respect to Mn (0.85 versus 0.45 wt%), Ni (0.84 versus 0.10 wt%) and Cr (0.39 versus 2.86 wt%). As already mentioned, Cr is expected to play a minor role because most of the Cr in GW8 is bound in carbides and the addition of 1% Cr to pure Fe did not change the ion-irradiation response reported in [15]. Figure 9 (c) shows that the ion-induced hardness increase observed for ANP-4 is significantly higher for fluences ≥ 0.1 dpa. The

large differences found can only be attributed to the higher Mn and/or Ni content. The result reported by Fujii et al. [13] for Fe-(Mn-Ni-Si) model alloys, namely ΔH(Fe-Mn-Si) ≈ ΔH(Fe-Mn-Ni-Si) >> ΔH(Fe-Ni-Si) between 0.1 and 0.5 dpa, indicates that it is the Mn instead of the Ni that enhances hardening in this range. Based on microstructure evidence, these authors suggested that the hardening is qualitatively consistent with Mn-enhanced loop formation. Indeed, other authors reported decoration of dislocation loops with Mn atoms for ion-irradiated Fe-1Mn (wt%) [49] and neutron-irradiated low-Cu RPV steels [50].

Finally, JFL and JRQ are compared in Figure 9 (d) for the sake of completeness. These widely known RPV steels differ in several respects including impurity levels and product form. Taking into account both the different P contents (0.004 versus 0.017 wt%) and the effect of P demonstrated in Figure 9 (b), we conclude that different P contents instead of different Cu contents are the dominant factor to explain the differences in ion-induced hardening between JFL and JRQ.

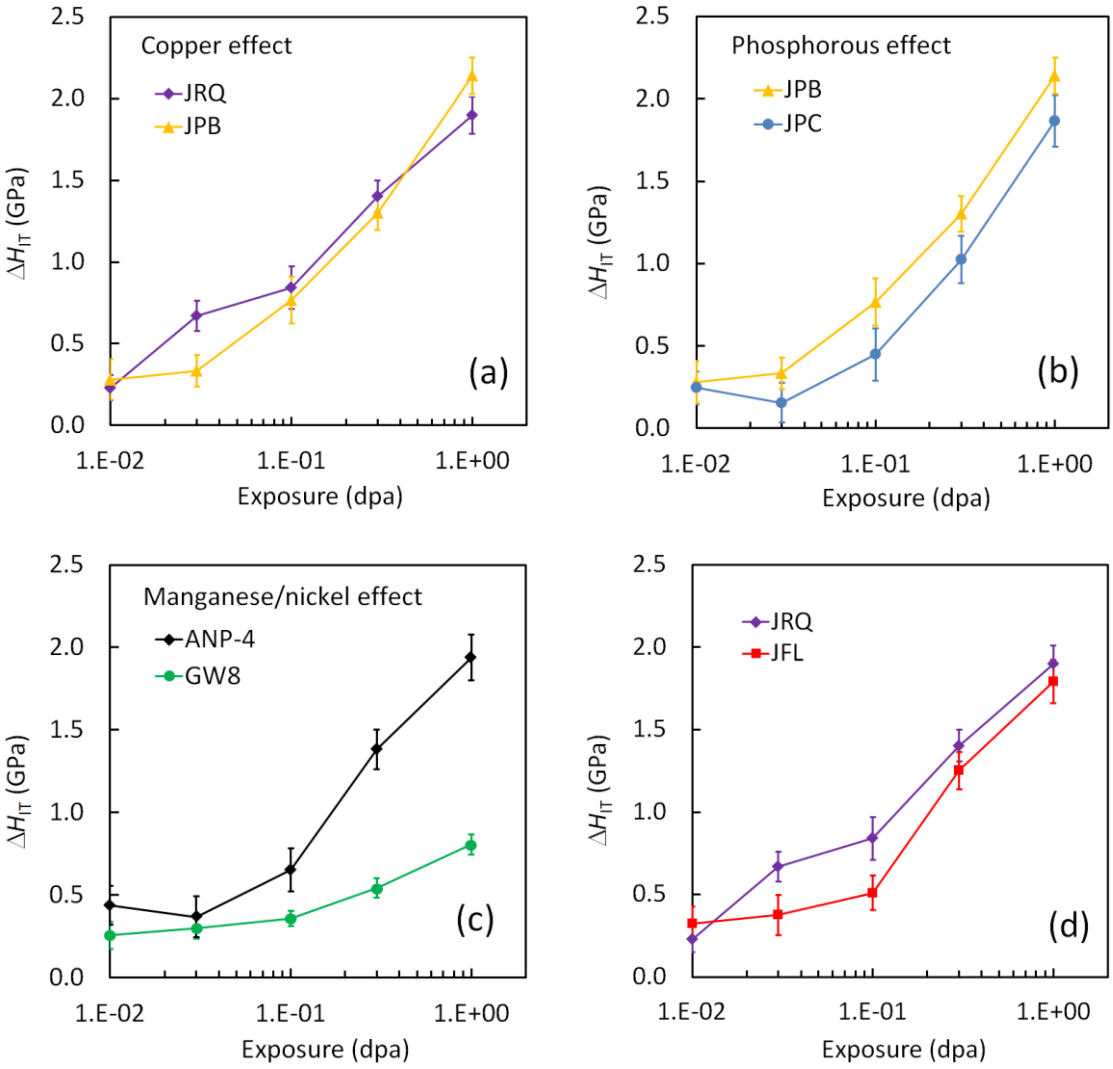

Figure 9. Pairwise comparison of the results of ion-induced hardening selected from Figure 7: comparison between the high-Cu steel JRQ and the low-Cu steel JPB with the same P concentration (a), comparison between the high-P steel JPB and the low-P steel JPC of otherwise identical composition (b), comparison between the high-Mn-Ni steel ANP-4 and the low-Mn-Ni steel GW8 of equal Cu content (c), and comparison between JRQ and JFL (d). The compositions can be found in Table 2.

5.3 Comparison with neutron-irradiation-induced hardening

The comparison of the ion-induced hardness increase of the present study with reported data on neutron-induced hardness changes is based on three ingredients:

- As shown above, the measured values of the nanohardness increase are associated to a well-defined ion exposure in terms of SRIM-dpa. These exposures are interpreted as approximately equivalent with the reported neutron fluences in terms of NRT-dpa [38].
- The increases of Vickers hardness reported for the neutron-irradiated RPV steels are converted into equivalent increases of nanoindentation hardness using an empirical linear regression obtained from a set of unirradiated materials (including the materials of this study as well as others). These materials were characterized by means of both Vickers hardness and nanoindentation. For the latter, the same method of analysis and the same reference contact depth as in the present study were used. The data are plotted in Figure 10. The conversion factor from ΔHV10 to ΔH_{IT} (in units of GPa) is 0.0114, which is remarkably close to the geometrical factor 0.01058 required to convert between indenter shapes.
- We restrict the comparison to neutron-irradiated samples of the same heats of RPV steels as those analyzed in the present study.

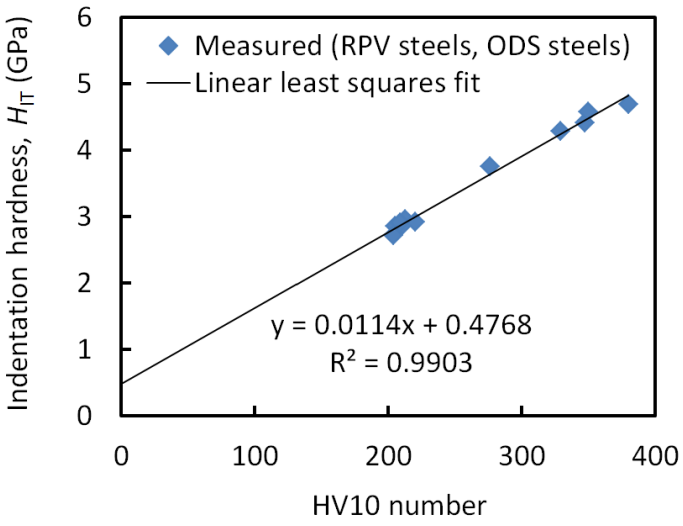

Figure 10. Indentation hardness versus Vickers hardness number HV10 for the unirradiated RPV steels of the present study and unirradiated ODS steels from a related study with indentation hardness estimated according to the same method and using the same reference contact depth.

The steels JRQ, JFL, JPB and JPC were irradiated with neutrons at the NPP Rheinsberg (Germany) in the late 80s (see [30] and references therein) and characterized by means of Vickers hardness measurements, tensile tests and small-angle neutron scattering [30,31,50]. The irradiation temperature was 255 °C. Samples irradiated up to three different neutron fluences are available. For the irradiation conditions of ANP-4, we refer to [33]. The irradiation temperature was 285 °C. Neutron irradiations of GW8 were performed at HFR Petten (LYRA irradiation rig, irradiation temperature 270 °C, 0.039 dpa) and Budapest Research Reactor (BAGIRA irradiation rig, irradiation temperature 280 °C, 0.312 dpa). The Vickers hardness of the latter materials was measured within the framework of the present study.

The ion- and neutron-induced hardness increases of the considered RPV steels are compared pairwise in Figures 11 (a) to (d) according to the same scheme as for the sole ion irradiations shown in Figure 9 (a) to (d). All results related to ion irradiations

are presented in terms of fitted power-law curves. Vickers hardness values of neutron-irradiated materials were converted to indentation hardness as described above.

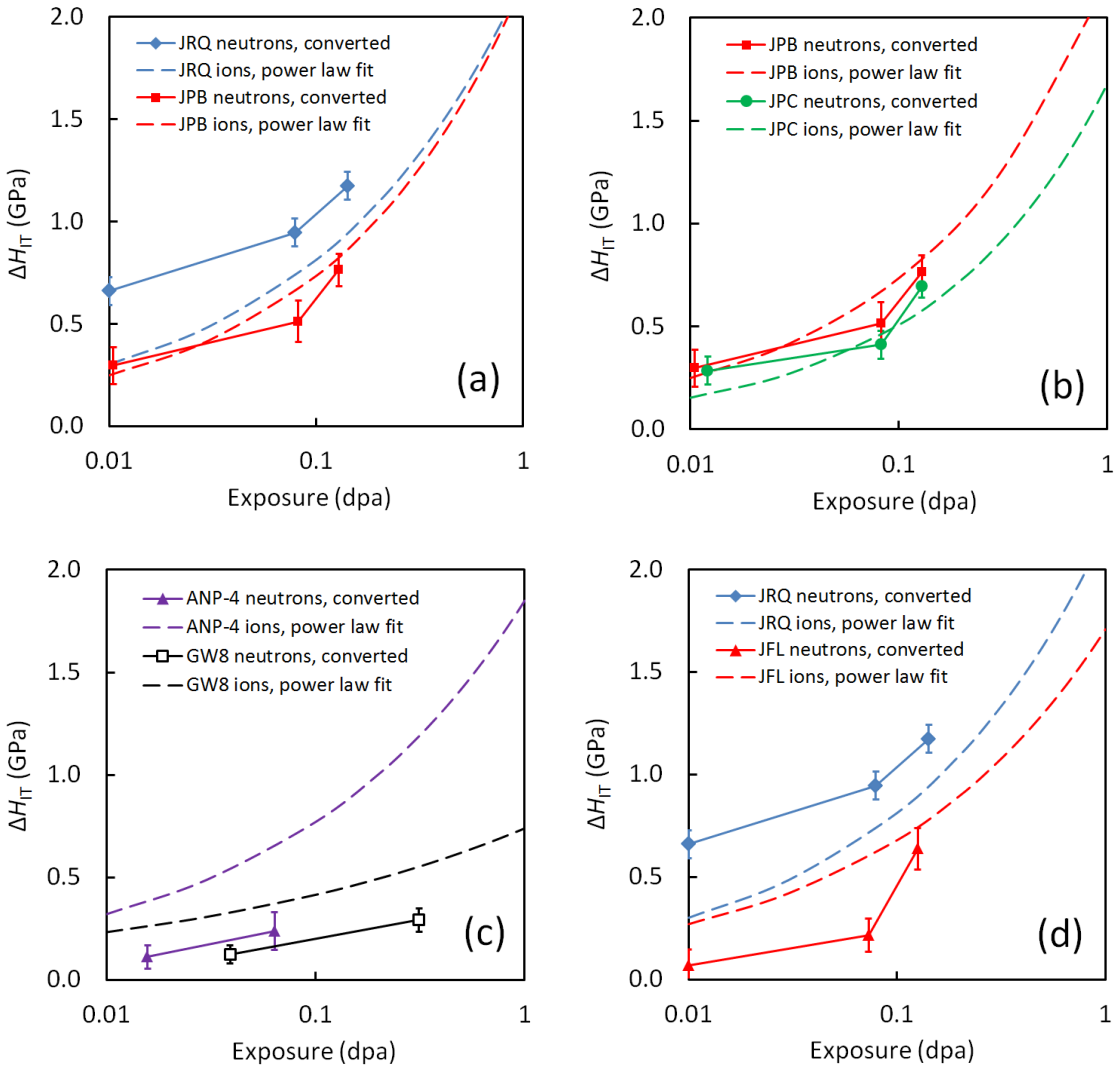

Figure 11. Pairwise comparison of the results of ion- and neutron-induced hardening: comparison between the high-Cu steel JRQ and the low-Cu steel JPB with the same P concentration (a), comparison between the high-P steel JPB and the low-P steel JPC of otherwise identical composition (b), comparison between the high-Mn-Ni steel ANP-4 and the low-Mn-Ni steel GW8 of equal Cu content (c), and comparison between JRQ and JFL (d).

A number of interesting details are observed on the basis of Figure 11 (a) to (d). In one case (high-Cu JRQ), the neutron-induced hardening is significantly stronger than the ion-induced hardening. In other cases (GW8 and low-Cu JFL and ANP-4) the opposite is true. For JPB and JPC, ions and neutrons give rise to similar hardness changes. A direct comparison of the effect of ions versus neutrons on hardening is not within the scope of the present study. However, it is obvious that the sources of the differences must be complex.

It seems to be more fruitful to see if and how compositional effects known from the field of neutron-irradiated RPV steels manifest themselves as a result of ion irradiations. Figure 11 (a) indicates that the Cu effect, which is relatively well understood for neutron irradiations, is much weaker (curves are much closer) for the same materials exposed to ion irradiations. The same observation was reported before by Watanabe et al. [17]. The pronounced differences in the response caused by ions and neutrons indicate that the dominant hardening mechanisms and, therefore, the dominant irradiation-induced nanofeatures are different.

Figure 11 (b) allows the P effect to be addressed. Contrary to the case of the Cu effect, ion irradiations seem to enhance the P effect in the sense that the curves for ions are more separated from one another than the corresponding curves for neutrons. Interestingly, the distance of separation is maintained over the whole dpa range. A possible interpretation of the effect of P in the case of ion irradiations was given in section 5.2.

The results in Figure 11 (c) are related to the Mn effect as already discussed for ions in section 5.2. The neutron-induced hardening is weaker than the ion-induced hardening for both ANP-4 and GW8. It seems that the Mn effect is more pronounced for ions than for neutrons. Under neutron irradiation, Ni was shown to give rise to the

formation of irradiation-induced clusters also in the absence of Mn [51]. More data at the neutron side are required for a sound discussion.

From the viewpoint of neutron irradiation, Figure 11 (d) is largely consistent with Figure 11 (a), which has been discussed above in terms of the Cu effect.

6. Conclusions

Nanoindentation was performed on six 5 MeV self-ion irradiated RPV steels. For the evaluation of the indentation-hardness profiles, we developed an analytic half-sphere model considering the indentation size, the softer substrate and the inhomogeneous displacement-damage profile as derived from SRIM calculations. This half-sphere model reproduces features of the indentation profiles and shows that the observed plateau region is a consequence of the damage profile caused by ion irradiation. For the determination of the actual hardness increase at 500 nm depth for all irradiation conditions, we propose – based on our half-sphere model – to use the indentation hardness increase measured at 200 nm contact depth. Thus, a direct assignment of measured hardness and displacement damage is established.

A detailed comparison of the ion-induced hardening among the selected RPV steels allows several effects of impurity and alloying elements to be identified:

- Comparison between ANP-4 and GW8 clearly reveals delayed hardening due to the ion-induced formation of Mn-segregated loops and/or Mn-Ni-rich precipitates. Results reported in the literature [15] indicate that Cr, which also differs for the two materials, plays a minor role. The Mn-Ni effect is similar or even stronger than for the case of neutron irradiation.

- Comparison between JRQ and JPB mainly reflects the effect of Cu. Contrary to

the pronounced effect of Cu observed for neutron-irradiated RPV steels, little or no effect of Cu is found for the case of ion irradiation, in particular in the range of higher displacement damage from 0.1 to 1 dpa. Cascade remnants and dislocation loops were reported in the literature [17] as candidate hardening features in the absence of Cu-rich precipitates.

- The difference between JPB and JPC indicates the influence of P on ion-induced hardening. This difference extends over the entire considered dpa range and is stronger than for the case of neutron irradiation. Our finding is consistent with a stabilization of cascade remnants by P segregation.

- The widely known RPV steels JRQ and JFL differ in both Cu and P. Given what was concluded above, the observed differences in the ion-induced hardening must be due to P instead of Cu, which is contrary to neutron irradiation.

The form and/or the parametrization of the proposed half-sphere model require further attention in order to allow the dpa dependence of ion-induced hardening to be derived from nanoindentation “from top” of only one ion-irradiated sample.

Acknowledgements

The use of HZDR Ion Beam Center facilities and the support by its staff is gratefully acknowledged. We kindly thank H. Hein for supply of unirradiated and neutron-irradiated material ANP-4 as well as M. Rossner for sample preparation. The reported research was performed within the EU-project SOTERIA. This project has received funding from the Euratom research and training programme 2014-2018 under Grant Agreement N° 661913.

References

[1] G. R. Odette, *On the dominant mechanism of irradiation embrittlement of reactor pressure vessel steels*, Scripta Metallurgica 17 (1983), pp. 1183–1188.

[2] G. R. Odette and G. E. Lucas, *Recent progress in understanding reactor pressure vessel steel embrittlement*, Rad. Eff. Def. Sol. 114 (1998), pp. 189-231.

[3] J. C. van Duysen and G. Meric de Bellefon, *60th Anniversary of electricity production from light water reactors: Historical review of the contribution of materials science to the safety of the pressure vessel*, J. Nucl. Mater. 484 (2017), pp. 209-227.

[4] D. J. Mazey, *Fundamental aspects of high-energy ion-beam simulation techniques and their relevance to fusion materials studies*, J. Nucl. Mater. 174 (1990), pp. 196-209.

[5] C. Abromeit, *Aspects of simulation of neutron damage by ion irradiation*, J. Nucl. Mater. 216 (1994), pp. 78-96.

[6] G. S. Was, *Fundamentals of radiation materials science: metals and alloys*, Springer-Verlag, Berlin, 2007.

[7] M. J. Fluss, P. Hosemann, and J. Marian, *Charged-particle irradiation for neutron radiation damage studies*, Characterization of Materials (2012), pp. 2111-2127.

[8] R. J. Bourcier, D. M. Follstaedt, M. T. Dugger, and S. M. Myers, *Mechanical characterization of several ion-implanted alloys: nanoindentation testing, wear testing and finite element modeling*, Nucl. Instr. Meth. Phys. Res. B 59-60 (1991), pp. 905-908.

[9] P. Hosemann, C. Vieh, R. R. Greco, S. Kabra, J. A. Valdez, M. J. Cappiello, and S. A. Maloy, *Nanoindentation on ion irradiated steels*, J. Nucl. Mater. 389 (2009), pp. 239-247.

[10] C. Heintze, F. Bergner, S. Akhmadaliev, and E. Altstadt, *Ion irradiation combined with nanoindentation as a screening test procedure for irradiation hardening*, J. Nucl. Mater. 472 (2016), pp. 196-205.

[11] P. M. Rice and R. E. Stoller, *The effect of solutes on defect distributions and hardening in ion-irradiated model ferritic alloys*, J. Nucl. Mater. 244 (1997), pp. 219-226.

[12] K. Fujii and K. Fukuya, *Characterization of defect clusters in ion-irradiated A533B steel*, J. Nucl. Mater. 336 (2005), pp. 323-330.

[13] K. Fujii, T. Ohkubo, and K. Fukuya, *Effects of solute elements on irradiation hardening and microstructural evolution in low alloy steels*, J. Nucl. Mater. 417 (2011), pp. 949-952.

[14] H. Watanabe, S. Masaki, S. Masubuchi, N. Yoshida, and Y. Kamada, *Radiation induced hardening of ion irradiated RPV steels*, J. Nucl. Mater. 417 (2011), pp. 932-935.

[15] K. Yabuuchi, M. Saito, R. Kasada, and A. Kimura, *Neutron irradiation hardening and microstructure changes in Fe–Mn binary alloys*, J. Nucl. Mater. 414 (2011), pp. 498-502.

[16] H.-H. Jin, J. Kwon, and C. Shin, *Evolution of radiation defect and radiation hardening in heat treated SA508 Gr3 steel*, Nucl. Instr. Meth. Phys. Res. B 319 (2014), pp. 24-28.

[17] H. Watanabe, S. Arase, T. Yamamoto, P. Wells, T. Onishi, and G. R. Odette, *Hardening and microstructural evolution of A533b steels irradiated with Fe ions and electrons*, J. Nucl. Mater. 471 (2016), pp. 243-250.

[18] Z. Yao, M. Hernández-Mayoral, M. L. Jenkins, and M. A. Kirk, *Heavy-ion irradiations of Fe and Fe-Cr model alloys Part 1: Damage evolution*

in thin-foils at lower doses, Phil. Mag. 88 (2008), pp. 2851-2880.

[19] M. Hernández-Mayoral, Z. Yao, M. L. Jenkins, and M. A. Kirk, *Heavy-ion irradiations of Fe and Fe-Cr model alloys Part 2: Damage evolution in thin-foils at higher doses*, Phil. Mag. 88 (2008), pp. 2881-2897.

[20] C. D. Hardie and S. G. Roberts, *Nanoindentation of model Fe–Cr alloys with self-ion irradiation*, J. Nucl. Mater. 433 (2013), pp. 174–179.

[21] G. S. Was, M. Hash, and R. G. Odette, *Hardening and microstructure evolution in proton-irradiated model and commercial pressure-vessel steels*, Phil. Mag. 85 (2006), pp. 703-722.

[22] W. D. Nix and H. Gao, *Indentation size effects in crystalline materials: a law for strain gradient plasticity*, J. Mech. Solids. 46 (1998) pp. 411-425.

[23] R. Kasada, Y. Takayama, K. Yabuuchi, and A. Kimura, *A new approach to evaluate irradiation hardening of ion-irradiated ferritic alloys by nano-indentation techniques*, Fus. Eng. Des. 86 (2011), pp. 2658-2661.

[24] Y. Takayama, R. Kasada, Y. Sakamoto, K. Yabuuchi, A. Kimura, M. Ando, D. Hamaguchi, and H. Tanigawa, *Nanoindentation hardness and its extrapolation to bulk-equivalent hardness of F82H steels after single- and dual-ion beam irradiation*, J. Nucl. Mater. 442 (2013), pp. 23-27.

[25] X. Liu, R. Wang, A. Ren, J. Jiang, C. Xu, P. Huang, W. Qian, Y. Wub, and C. Zhang, Evaluation of radiation hardening in ion-irradiated Fe based alloys by nanoindentation, J. Nucl. Mater. 444 (2014), pp. 1-6.

[26] P. Hosemann, D. Kiener, Y. Wang, and S. A. Maloy, *Issues to consider using nano indentation on shallow ion beam irradiated materials*, J. Nucl. Mater. 425 (2012), pp. 136-139.

[27] X. Xiao, Q. Chen, H. Yang, H. Duan, and J. Qu, *A mechanistic model for depth-dependent hardness of ion irradiated metals*, J. Nucl. Mater. 485 (2017), pp. 80-89.

[28] H.-S. Kim, D.-H. Lee, M.-Y. Seok, Y. Zhao, W.-J. Kim, D. Kwon, H.-H. Jin, J. Kwon, and J. Jang, *A novel way to estimate the nanoindentation hardness of only-irradiated layer and its application to ion irradiated Fe-12Cr alloy*, J. Nucl. Mater. 487 (2017), pp. 343-347.

[29] A. Ulbricht, and J. Böhmert, *Small angle neutron scattering analysis of the radiation susceptibility of reactor pressure vessel steels*, Physica B 350 (2004), pp. 483-486.

[30] A. Ulbricht, J. Böhmert, and H.-W. Viehrig, *Microstructural and Mechanical Characterization of Radiation Effects in Model Reactor Pressure Vessel Steels*, J. ASTM Int. 2 (2005) 10, Paper ID JAI12385.

[31] F. Bergner, A. Ulbricht, and H.-W. Viehrig, *Acceleration of irradiation hardening of low-copper reactor pressure vessel steel observed by means of SANS and tensile testing*, Phil. Mag. Lett. 89 (2009), pp. 795-805.

[32] A. Wagner, F. Bergner, A. Ulbricht, and C. D. Dewhurst, *Small-angle neutron scattering of low-Cu RPV steels neutron-irradiated at 255°C and post-irradiation annealed at 290°C*, J. Nucl. Mater. 441 (2013), pp. 487-492.

[33] E. Altstadt, E. Keim, H. Hein, M. Serrano, F. Bergner, H.-W. Viehrig, A. Ballesteros, R. Chaouadi, and K. Wilford, *FP7 Project LONGLIFE, Overview of results and implications*, Nucl. Eng. Des. 278 (2014), pp. 753-757.

[34] G. R. Odette and B. D. Wirth, *A computational microscopy study of nanostructural evolution in irradiated pressure vessel steels*, J. Nucl. Mater. 251 (1997), pp. 157-171.

[35] IAEA, *Manufracturing history and mechanical properties of japanese materials provided for the international atomic energy agency*, CRP Sub-Committee Japan Welding Engineering Society, IAEA, Vienna, October 1986.

[36] H.-W. Viehrig, M. Scibetta, and K. Wallin, Application of advanced master curve approaches on WWER-440 reactor pressure vessel steels, Int. J. Press. Vessels Pip. 83 (2006), pp. 584-592.

[37] J. F. Ziegler, M. D. Ziegler, and J. P. Biersack, *SRIM - The stopping and range of ions in matter (2010)*, Nucl. Instr. Meth. Phys. Res. B 268 (2010) pp. 1818-1823.

[38] R. E. Stoller, M. B. Toloczko, G. S. Was, A. G. Certain, S. Dwaraknath, and F. A. Garner, *On the use of SRIM for computing radiation damage exposure*, Nucl. Instr. Meth. Phys. Res. B 310 (2013), pp. 75-80.

[39] M. R. Maughan, A. A. Leonard, D. D. Stauffer, and D. F. Bahr, *The effects of intrinsic properties and defect structures on the indentation size effect in metals*, Phil. Mag. 97 (2017), pp. 1902-1920.

[40] T. S. Byun and K. Farrell, *Irradiation hardening behavior of polycrystalline metals after low temperature irradiation*, J. Nucl. Mater. 326 (2004), pp. 86-96.

[41] B. Jönsson and S. Hogmark, *Hardness measurements of thin films*, Thin Solid Films 114 (1984), pp. 257-269.

[42] A. J. Wilkinson and D. Randman*, Determination of elastic strain fields and geometrically necessary dislocation distributions near nanoindents using electron back scatter diffraction*, Phil. Mag. 90 (2010), pp. 1159-1177.

[43] Z. Xue, Y. Huang, K. C. Hwang, and M. Li, *The influence of the indenter tip radius on the micro-indentation hardness*, J. Eng. Mater. Technol. 124 (2002), pp. 371-379.

[44] X. Hou and N. M. Jennett, *Application of a modified slip-distance theory to the indentation of single-crystal and polycrystalline copper to model the interactions between indentation size and structure size effects*, Acta Mater. 60 (2012), pp. 4128-4135.

[45] T. A. Laursen and J. C. Simo, *A study of the mechanics of microindentation using finite elements*, J. Mater. Res. 7 (1992), pp. 618-626.

[46] D. Chicot and J. Lesage, *Absolute hardness of films and coatings*, Thin Solid Films 254 (1995), pp. 123-130.

[47] J. Kocik, E. Keilova, J. Cizek, and I Prochazka, *TEM and PAS study of neutron irradiated VVER-type RPV steels*, J. Nucl. Mater. 303 (2002), pp. 52-64.

[48] L. Malerba, G. J. Ackland, C. S. Becquart, G. Bonny, C. Domain, S. L. Dudarev, C.-C. Fu, D. Hepburn, M. C. Marinica, P. Olsson, R. C. Pasianot, J. M. Raulot, F. Soisson, D. Terentyev, E. Vincent, and F. Willaime, *Ab initio calculations and interatomic potentials for iron and iron alloys: Achievements within the Perfect Project,* J. Nucl. Mater. 406 (2010), pp. 7-18.

[49] E. Meslin, B. Radiguet, and M. Loyer-Prost, *Radiation-induced precipitation in a ferritic model alloy: An experimental and theoretical study*, Acta Mater. 61 (2013), pp. 6246–6254.

[50] A. Wagner, *Long-term irradiation effects on reactor pressure vessel steels, investigation on the nanometer scale*, Ph.D. diss., Martin-Luther-Universität Halle-Wittenberg, 2017.

[51] F. Bergner, A. Ulbricht, M. Hernandez-Mayoral, and P. K. Pranzas, *Small-angle neutron scattering study of neutron-irradiated iron and an iron–nickel alloy*, J. Nucl. Mater. 374 (2008), pp. 334-337.